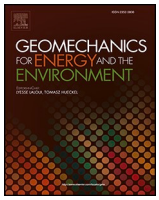
Geomechanics for Energy and the Environment 48 (2026) 100924



Contents lists available at ScienceDirect

Geomechanics for Energy and the Environment

journal homepage: www.elsevier.com/locate/gete



# Fracture closure in pure quartz sandstone at low stress and temperature

Harald Milsch [a,*], Chaojie Cheng [b], Renchao Lu [c], Haibing Shao [c], Olaf Kolditz [c,d]

[a] GFZ Helmholtz Centre for Geosciences, Geoenergy, Potsdam, Germany
[b] KIT Karlsruhe Institute of Technology, Applied Geosciences, Karlsruhe, Germany
[c] Helmholtz Centre for Environmental Research - UFZ, Leipzig, Germany
[d] Technical University Dresden, Dresden, Germany

ARTICLE INFO

Editors-in-Chief: DR P Papanastasiou

*Keywords:*
Fluid-rock interactions
Sandstone
Pressure solution
Stress corrosion cracking
Free face dissolution
Fracture permeability

ABSTRACT

The purpose of this paper is to report on the outcome of a continuous long-term flow-through experiment conducted on a fractured pure quartz sandstone (Fontainebleau) at 60 °C. Changes in effective pressure (1, 17, and 29 MPa) and pore fluid composition (deionized water and Si-rich solution) were sequentially imposed to investigate their respective effect on time-dependent fracture closure. Hydraulic fracture aperture, as derived from permeability measurements, showed to decrease substantially by about 50% within the 120 days of the experiment. Based on complementary analyses of the effluent Si concentration and microstructural investigations, it is suggested that, mechanistically, pressure solution, stress corrosion cracking, and free face dissolution contribute to the overall aperture decrease. However, as the fracture morphology evolves with time, the deformation mechanisms that are driven by diffusion and/or stress (i.e., pressure solution and stress corrosion cracking) may deactivate, yielding a significant decrease in the fracture closure rate. The study suggests follow-up experiments to quantitatively decipher the relative importance of the complex and coupled processes affecting fracture aperture and permeability.

## 1. Introduction

Within the Earth's upper crust, rock fractures are important structural features as they permit effective fluid transport. Fluid-rock interactions proceeding therein may provoke time-dependent deformation associated with permeability changes (e.g., [1–6]). Mechanistically and in the presence of fluids, changes in fracture aperture are mainly governed by three grain-scale processes, i.e., pressure solution [7–10], free face dissolution (and/or precipitation) [2,11], and stress corrosion cracking [12–14], which constitute a complex coupling of mechanical, hydraulic, thermal, and chemical mechanisms.

Pressure solution (PS) implies a mass transfer from highly stressed contact asperities to the free pore fluid along a water film within the solid-solid contact interfaces [15–19]. The driving force of this process is well-known from a thermodynamic perspective in that a non-hydrostatic stress increases the chemical potential gradient within the fluid between the stressed solid contacts and the open pore space [8,20]. In the past, a number of laboratory studies were carried out with pure quartz aggregates at relatively high temperatures (e.g., 150–600 °C in [15,21–24]) but also with single contacts [25–28]. The observed time-dependent porosity reduction or indentation depth as well as the contact microstructures were found to be attributable to PS, particularly at the early stages of deformation.

Free face dissolution (FFD) is driven by hydro-thermo-chemical processes and occurs on the parts of the fracture walls that are exposed to the pore fluid, where the minerals are subjected to a hydrostatic pore pressure. This mechanism causes a solid phase removal within the fracture void and thus, in the absence of precipitation, an enlargement of the fracture aperture (e.g., [11,29]).

Stress corrosion cracking (SCC) results in subcritical crack growth, where the fluid-rock interaction occurs preferentially at the crack tips between the chemically reactive fluid and the strained atomic bonds of the solid, leading to crack propagation [14,30,31]. This process is one of the major mechanisms of fluid-assisted brittle rock creep, where time-dependent deformation is observed at stresses lower than the short-term rock strength [12,13,32]. SCC, when it occurs at the highly stressed contact asperities in fractures, may lead to their stepwise crushing or failure and thus to fracture closure [33].

When a fluid flows through a rock fracture at some constant pressure and temperature conditions the aforementioned processes may operate simultaneously. To date, a limited number of longer-term flow-through experiments were carried out to investigate the evolution of

* Corresponding author.
*E-mail address:* milsch@gfz.de (H. Milsch).

https://doi.org/10.1016/j.gete.2026.100924
Received 19 February 2026; Received in revised form 15 October 2026; Accepted 31 October 2026
Available online 2 November 2026
2352-3808/© 2026 The Author(s). Published by Elsevier Ltd. This is an open access article under the CC BY license (http://creativecommons.org/licenses/by/4.0/).
Open access funding enabled and organized by Projekt DEAL.

permeability mediated by fluid-rock interactions[2–5,11,29,34–42]. A time-dependent permeability decline was observed in most cases being favored by elevated temperatures. However, deciphering the respective mechanisms that dominate the overall evolution of fracture aperture requires continued investigational efforts, particularly for the case of low temperatures.

In this spirit, a long-term (~120 days) continuous flow-through experiment was performed at constant temperature (60 °C) on a pure quartz sandstone containing one single rough fracture, varying effective pressure (and thus fracture normal stress) as well as fluid composition. Complemented with microstructural investigations, this study attempts to relate the experimental and analytical observations to the respective occurrence of the three grain-scale mechanisms outlined above, i.e., PS, FFD, and SCC.

## 2. Materials and methods

### 2.1. Sample material and fluids

The cylindrical rock sample used for the flow-through experiment measured 30 mm in diameter and 40 mm in length and was drilled from a larger Fontainebleau sandstone block, quarried near Fontainebleau, France. This particular type of Fontainebleau sandstone (Fig. 1 and Figure S1 in the Supplementary Materials) is composed of > 99.5 wt% of quartz and is characterized by a porosity of ~2.5% and a matrix permeability in the order of $10^{-18}$ $m^2$, as evidenced by previous permeability measurements. Matrix permeability was measured in a (routine) gas permeameter at GFZ under a confining pressure of approximately 10 MPa and at ambient temperature (ca. 20 °C) with four different upstream pore pressures permitting to apply the Klinkenberg correction. Using a Brazilian test setup, the sample was split into two halves along its principal axis (Fig. 1a and b).

To prevent the fracture from immediate closure upon pressurization, a 200 μm displacement between the two halves was introduced manually and locked using two polyether ether ketone (PEEK) spacers (Fig. 2a). Each of the spacers contains a precisely machined step of 200 μm to keep the two sample halves axially offset during the experiment. It should be noted though that it cannot be independently verified that the offset was precisely 200 μm, when the assembly was in the pressure vessel at confining pressure. Afterwards, the sample was further assembled as shown in Figs. 1c and 2a.

Two types of fluids were used during the experiment: (a) deionized water and (b) a water-based and synthetic solution enriched in silica. The latter aimed to investigate if a fluid containing the dissolved counterpart of the dominant rock mineral, i.e., quartz, affects the rate at which potential changes in hydraulic aperture occur. The use of both fluids thus represents an end member scenario. The silica solution was prepared by diluting and neutralizing an Si standard solution (i.e., 1000 mg/l of Si and 0.5 mol/l of NaOH) to an Si concentration of ~$2.60 \times 10^{-4}$ mol/l and a pH value of ~6.9, which is close to the solubility of quartz in water at 60 °C and neutral pH conditions, i.e., $3.03 \times 10^{-4}$ mol/l[43]. The density and dynamic viscosity of deionized water used to evaluate the raw data for hydraulic aperture were taken from tabulated values at 60 °C and 1 MPa provided by the National Institute of Standards and Technology (NIST) (https://webbook.nist.gov/chemistry/fluid/) assuming pure water, yielding 983.59 kg/$m^3$

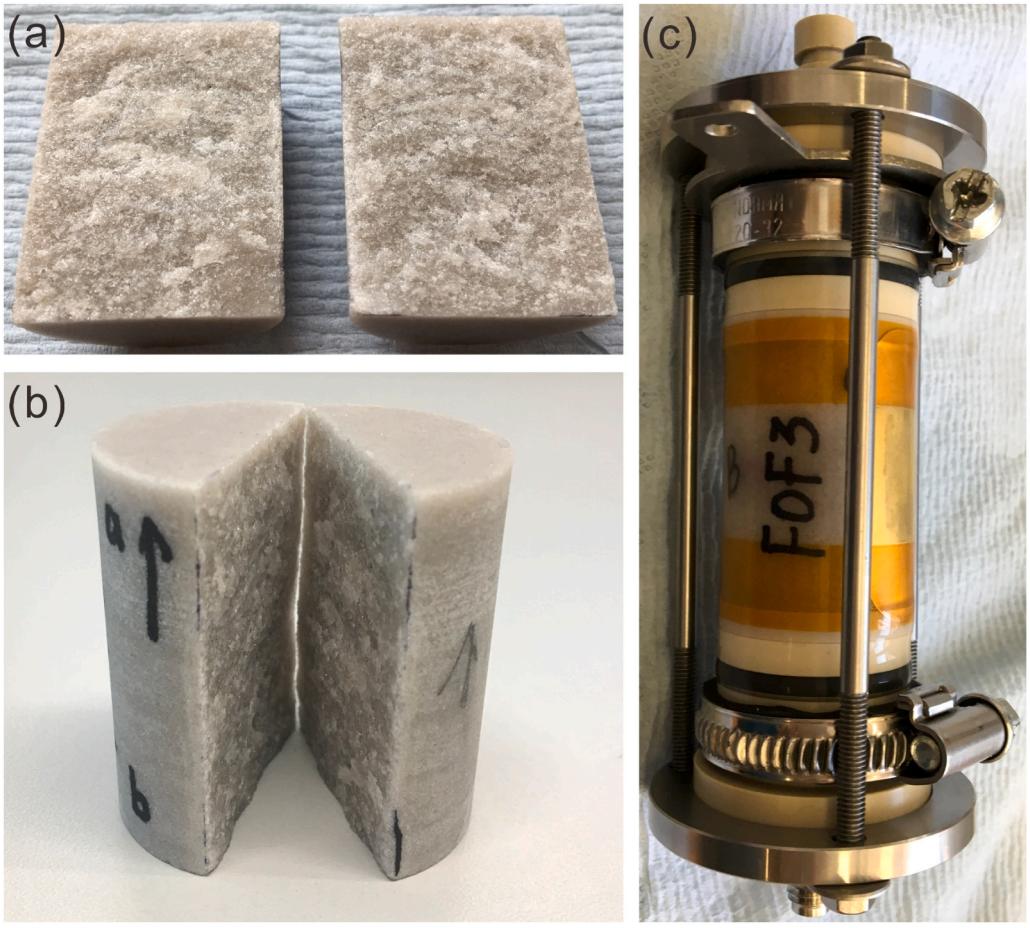



**Fig. 1.** (a), (b) Photographs of the rock sample used for the experiment. The artificial tensile fracture was generated with a Brazilian test setup at a low displacement rate of $2 \times 10^{-6}$ m/s to minimize a risk of edge damage; (c) specimen assembly of the fractured sample with a relative offset of 200 μm along its length, jacketed with a heat-shrink tubing and additional sealing parts. The sample is 30 mm in diameter and 40 mm in length.

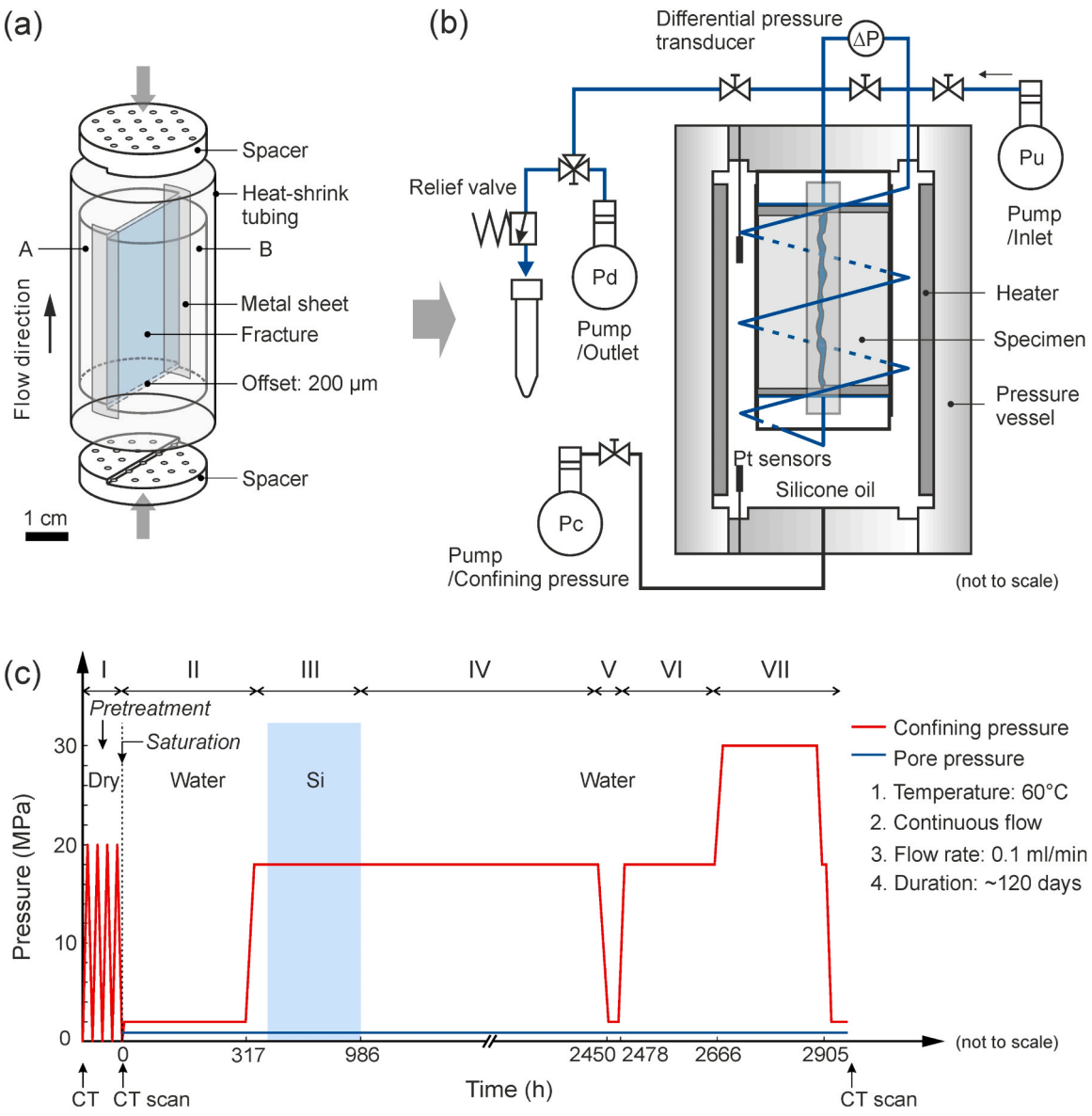



**Fig. 2.** Schematic illustration of the experimental setup and the experimental procedures: (a) the specimen halves were misaligned by 200 µm using PEEK spacers and jacketed with a heat-shrink tubing where two metal sheets placed onto the fracture void prevented the jacket from punching upon pressurization. (b) The flow-through apparatus used for the long-term experiment consists of a hydrostatic confining pressure system and a separate pore fluid system. All wetted parts of the pore fluid system are made of Hastelloy C-276 to avoid any formation of corrosion products during an experiment. Pore pressure was maintained constant at 1 MPa either by a relief valve (used for fluid sampling) or by the downstream pump (used for measuring permeability). (c) Schematic of the experimental procedures, conditions, and stages of the entire experiment. The second CT scan was conducted right before the start of the long-term flow-through experiment referring to t = 0. The first CT scan was conducted after specimen assembly and before preconditioning (i.e., stage I). The duration of stage I is not to scale on the x-axis.

and 0.4666 mPa·s, respectively. As the prepared silica solution is water-based and highly diluted, its density and viscosity were assumed to be identical to that of pure water at the experimental pT-conditions.

### 2.2. Experimental procedures

The entire experiment comprised 7 sequential stages and had a total duration of ~120 days. The purpose of these stages, detailed in the following, was to systematically and mechanistically investigate the possible effects of changes in stress and fluid composition on the time-dependence of hydraulic fracture aperture and thereby fracture permeability.

**Stage I:** During a pretreatment conducted in an autoclave (Berghof BR-300), the dry and sealed specimen assembly was pressurized with argon gas four times up to 20 MPa to minimize irreversible, purely mechanical deformation at later stages.

**Stage II:** The assembly was vacuum-dried at 60 °C in an oven and then saturated with deionized water in a desiccator. Subsequently, it was mounted in a flow-through apparatus (Fig. 2b), described in detail by Milsch et al.[44]. Throughout the experiment, the sample was continuously flown through at a constant flow rate of 0.1 ml/min and at a constant temperature of 60 °C. The downstream fluid pressure $p_p$ was also kept constant at 1 MPa and the confining pressure $p_c$ was first set to 2 MPa.

**Stage III:** The confining pressure was increased to 18 MPa and the deionized water, as injected so far, was replaced by the synthetic silica solution approximately 100 h afterwards.

**Stages IV-VII:** The silica solution was again replaced by deionized water, maintaining confining pressure at 18 MPa (**IV**). An unloading-reloading cycle was then performed, during which confining pressure

was decreased to 2 MPa (**V**). After reloading, the confining pressure was, again, held constant at 18 MPa (**VI**) and later on was further increased to 30 MPa (**VII**). Afterwards, the experiment was terminated by decreasing temperature, complete unloading, and disassembly of the specimen.

The entire experimental sequence comprising the duration of each of the stages is sketched in Fig. 2c. The transitions from stages II to III and VI to VII aimed at deciphering an effect of confining pressure changes on time-dependent fracture closure at nominally constant fluid chemistry. In contrast, stage III and its transition to stage IV meant to investigate a potential response of the fracture to changes in fluid chemistry at constant pressure. The initial hypothesis was that when increasing effective pressure, i.e., going from stage II to III, pressure solution could be accelerated but decelerated when the Si concentration is increased, respectively increasing and decreasing the rate at which hydraulic aperture would change. In contrast, when going from stage III to IV, pressure solution should, again, be accelerated. Finally, the purpose of stage V was to verify, by unloading, if a fluid enriched in Si was trapped in the contact asperities. Flushing out such a fluid may reset the chemical fluid conditions in the contacts and thereby alter the rate at which a change in fracture aperture would occur.

During the entire flow-through experiment (i.e., stages II-VII), about 3 ml of effluent was sampled from the relief valve at a constant flow rate of 0.1 ml/min once every 24 h. In stage V, one fluid sample was collected right after unloading to 2 MPa and another one after 28 h at the same stress. The collected effluent samples, as well as reference samples of both deionized water and the silica solution, were analyzed by inductively coupled plasma optical emission spectrometry (ICP-OES) at a wavelength of 251.611 nm in the geochemical laboratory at the Technical University (TU) Berlin, Germany.

Permeability was always measured after effluent sampling approximately every two days. The setup used two syringe pumps of type ISCO 260D with excellent flow rate stability. The upstream pump was used in constant flow rate mode and the downstream pump in constant pressure mode. Flow rate precision is 0.001 ml/min and inflow-outflow conservation was verified regularly by comparing the flow-rate readings on the pump controller displays of both pumps on a daily basis. The differential pressure transducer (Omega PXM409–035BDWUI) has a 0–3.5 MPa range with a stated accuracy of 0.08% FS. In order to increase the differential pore pressure into a range that is measurable for the differential pressure transducer, the flow rate was shortly increased to 2–4 ml/min during permeability testing, where one measurement took approximately 2–4 mins to reach steady-state. In this flow rate range, the differential pressure was observed to vary between 0.025 and 0.36 bar and the pulsation of the downstream pump was + /- 0.05 ml/min at most, thus + /- 2.5% of the set flow rate at maximum. Afterwards, the flow rate was immediately restored to 0.1 ml/min, accompanied by switching the outlet port from the downstream pump to the relief valve (Fig. 2b). It is noted that due to the long duration of the experiment and the need to perform the permeability measurements manually meant that the actual intervals were not always 48 h, e.g., during weekends and public holidays. In particular, the 236-h gap between 1778 and 2014 h resulted from a holiday absence. Here, flow was ongoing but no permeability measurements were performed. For the exact schedule of permeability measurements, we refer to the data table in the Supplementary Materials.

From the measured sample permeability, hydraulic aperture $b_h$ was calculated by applying the so-called "cubic law"[45], with the reasonable assumption that matrix permeability can be neglected:

$$b_h = \sqrt[3]{\frac{12\mu L \bullet Q_v}{W\Delta P}}, \tag{1}$$

where $\mu$ (Pa/s) is the dynamic fluid viscosity, $W$ and $L$ (m) are the width and length of the fracture, $\Delta P$ (Pa) is the differential pressure between the upstream and downstream sides of the sample, and $Q_v$ ($m^3$/s) is the flow rate at vessel temperature. The hydraulic aperture calculation is thus based on the assumption of laminar flow through parallel plates, which is different from the mechanical (geometric) separation of the fracture surfaces. The deviation is more significant when the fracture aperture is small and the fracture surface is rough[46].

Given the temperature difference between the vessel and the upstream syringe pump. $Q_v$, was calculated from the measured flow rate $Q_p$ in the syringe pump as,

$$Q_v = \frac{Q_p \rho_p}{\rho_v} \tag{2}$$

where $\rho_p$ and $\rho_v$ (kg/$m^3$) are the fluid densities at room temperature (25 °C) and vessel temperature (60 °C), respectively.

### 2.3. Microstructural investigations

Complementing the flow-through experiment, different microstructural investigations were performed. The surface topographies of the two specimen halves were measured before stage I and after the completion of the experiment using white light interferometry (Keyence VR-3200). The length resolution in the horizontal x-y plane and along the vertical z-axis is 23.518 μm and 1 μm, respectively, allowing for high-quality imaging and a quantitative geometric surface analysis (Figure S2). Three X-ray micro-computed tomography (μCT) scans (Phoenix Nanotom M) were conducted at different experimental stages (Fig. 2c). In order to obtain comparable results, all scans were performed with the dried but jacketed sample at atmospheric conditions using the same scanning parameters (i.e., timing: 750 ms; voltage: 120 kV; current: 90 μA; voxel size: 20.63 μm), yielding a total of 1080 two-dimensional slices. The 3-D μCT models of the sample were then generated by using all of the 1080 slices of each scan. Finally, after the experiment, the fracture surfaces were carbon-coated for high magnification scanning electron microscopy (SEM) imaging (ZEISS Ultra Plus) of fracture surface features.

## 3. Results

### 3.1. Hydraulic aperture and effluent Si concentration

Fig. 3 shows the evolution of hydraulic aperture and effluent Si concentration throughout the experiment. All experimental data are documented in Cheng et al.[47]. The total cumulative reduction in hydraulic fracture aperture was 30.9 μm or approximately 50%, with respect to the initial aperture. To assess the interpretability of hydraulic aperture changes individual, neighboring permeability measurements (e.g., at 1489 h and 1513 h) can be compared yielding a difference of 0.61 μm. For the three measurements between 2305 h and 2352 h, hydraulic aperture remained nearly constant. Consequently, the uncertainty of hydraulic aperture, as derived from permeability measurements, can be assumed to be around 0.5 μm. Moreover, the effluent was observed to be enriched in Si throughout the experiment in comparison to the injection fluid (Fig. 3a). The uncertainty of the ICP-OES data can best be assessed from the scatter of the influent Si concentration in Fig. 3 or the data file provided in the Supplementary Materials. For the pure (DI) water stages, evidently, the Si concentration in the effluent is always well above the influent baseline, even when taking the influent data scatter into account. For stage III, the Si concentration is significantly higher and so is the scatter of the influent Si concentration.

**Stage II:** The hydraulic aperture decreased from 60.7 to 55.6 μm at an effective pressure of 1 MPa. Since the start of this stage, the sampled effluent Si concentration was well above the one of the injection fluid but, in the same manner as the hydraulic aperture, continuously decreased (Fig. 3b).

**Stage III:** The effective pressure increase to 17 MPa had an immediate (i.e., elastic) effect on the hydraulic aperture, which underwent a

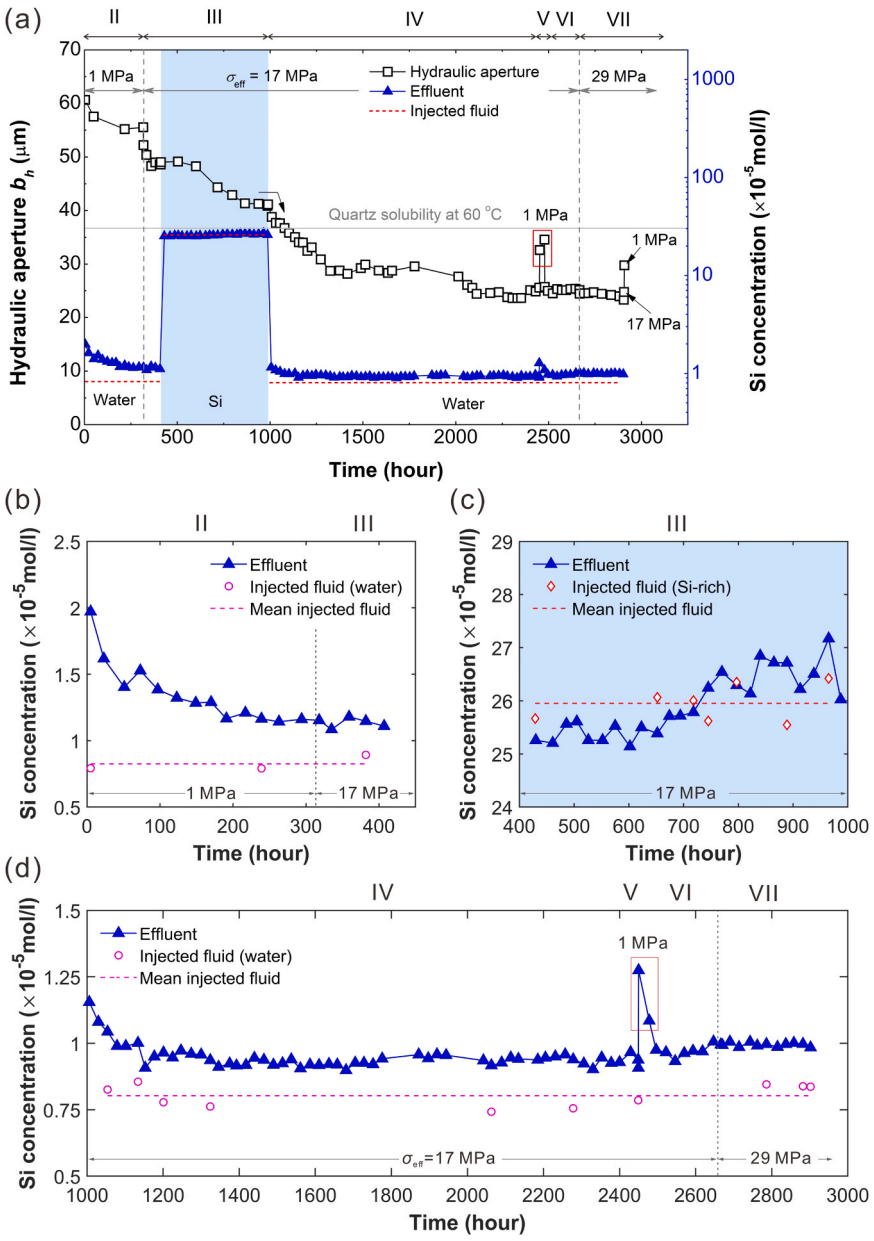



**Fig. 3.** (a) Evolution of hydraulic aperture as well as injection fluid and effluent Si concentrations during the entire flow-through experiment. Details of the Si concentrations during different experimental stages: (b) stage II and early stage III; (c) stage III; (d) stages IV to VII.

decrease by 3.4 μm. During the following 42 h, the hydraulic aperture continuously decreased to 48.6 μm. However, despite the significantly higher normal contact stress, no immediate effect on the effluent Si concentration was observed (Fig. 3b). At 412 h, the deionized water in the sample void space was exchanged with the silica solution as the injection fluid. This fluid exchange did not affect the hydraulic aperture during the following 189 h. From 601 h onwards, the hydraulic aperture started to decrease and then converged to a constant value of 40.9 μm towards the end of this stage at 986 h. Despite larger fluctuations, the Si concentration of the effluent during the first half of this stage was slightly below the one of the injection fluid and then increased to a value slightly higher than the latter for the second half (Fig. 3c).

**Stage IV:** The silica solution was again exchanged for deionized water, which caused the hydraulic aperture to decrease remarkably with time at constant effective pressure. After undergoing a continuous decrease to 25.0 μm, the hydraulic aperture remained approximately constant after 2100 h. However, the rate at which this decrease occurred shows two distinct segments with a transition after approximately 1300 h. Similarly, the effluent Si concentration gradually decreased until 1300 h but then remained more or less constant at 9.4 × $10^{-6}$ mol/l until the end of this stage (Fig. 3d).

**Stage V:** When confining pressure was decreased from 18 MPa to 2 MPa, the hydraulic aperture instantaneously increased to approximately 33 μm and the effluent Si concentration showed a pronounced peak of about 1.3 × $10^{-5}$ mol/l (Fig. 3d). Within the next 28 h, the concentration decreased again to 1.1 × $10^{-5}$ mol/l.

**Stage VI:** Reloading confining pressure to 18 MPa restored hydraulic aperture to 25 μm and the effluent Si concentration returned to the level observed at the end of stage IV (Fig. 3d). Both parameters then remained approximately constant until the end of this stage.

**Stage VII:** A further increase in effective pressure to 29 MPa was applied, which caused the hydraulic aperture to elastically decrease by less than 1 μm with no significant change afterwards. Compared to stage VI, a slightly higher effluent Si concentration can be noticed, which, however, then remained constant until the end of the experiment (Fig. 3d). Stage VII was not foreseen when the experiment was started

ca. 3.5 months before. As hydraulic aperture did not change during the preceding ca. 25 days at 17 MPa effective pressure, it was decided to increase confining pressure as a last step to investigate how the fracture would react to that change regarding, both, the hydraulic aperture evolution and the Si signal in the effluent. It is noted that this effective pressure exceeds the maximum pressure applied during preconditioning (i.e., stage I). After approximately 2900 h (i.e., 120 days), the experiment was terminated by unloading effective pressure to 17 MPa and further to 1 MPa yielding a final hydraulic aperture of 29.8 μm, i.e., approximately 50% of the initial aperture.

### 3.2. Microstructure of the fracture and contacting asperities

Fig. 4 shows the evolution of the contact area of the fracture obtained from μCT imaging as well as the microstructure of contacting asperities observed by SEM. Fracture voids (Fig. 4a) were extracted from each model and subsequently projected onto the selected datum plane to obtain the 2-D projections shown in Fig. 4b. The contact areas clearly indicate the serial changes resulting from purely mechanical compaction during stage I and irreversible, fluid assisted deformation at later stages, respectively. Mechanical compaction results mainly in new contact points, increasing from 659 to 5252 resolvable contacts, rather than in enlarging the area of the existing contact asperities (Figure S3). After the experiment, the fracture deformation, accompanied by the remarkable decrease in hydraulic aperture, resulted in a significant increase of the total contact area $A_c$ and thereby the contact area ratio $R_c = A_c / (W\,L)$ from 0.04 to 0.12. As the number of contacts had decreased from 5252 to 4210 during the experiment, this indicates that some of the contacts in close vicinity may have merged[48]. From SEM imaging (Fig. 4c), two distinct types of contacts were identified, which are pervasive in both sample halves: (i) nominally flat or undulating contacts with some internal roughness at the micrometer scale (left) and (ii) truly rough contacts with obvious signs of micro-cracking or grain crushing (right).

The contact areas identified from the μCT data are subject to the spatial resolution of the scans with a voxel size of 20.63 μm. Smaller structural features thus cannot be resolved reliably. In addition, all μCT scans were performed on the dried but jacketed specimen at ambient conditions thus without confining pressure. Therefore, the fracture geometry obtained from μCT does not represent the actual aperture and contact configuration under the experimental stress conditions.

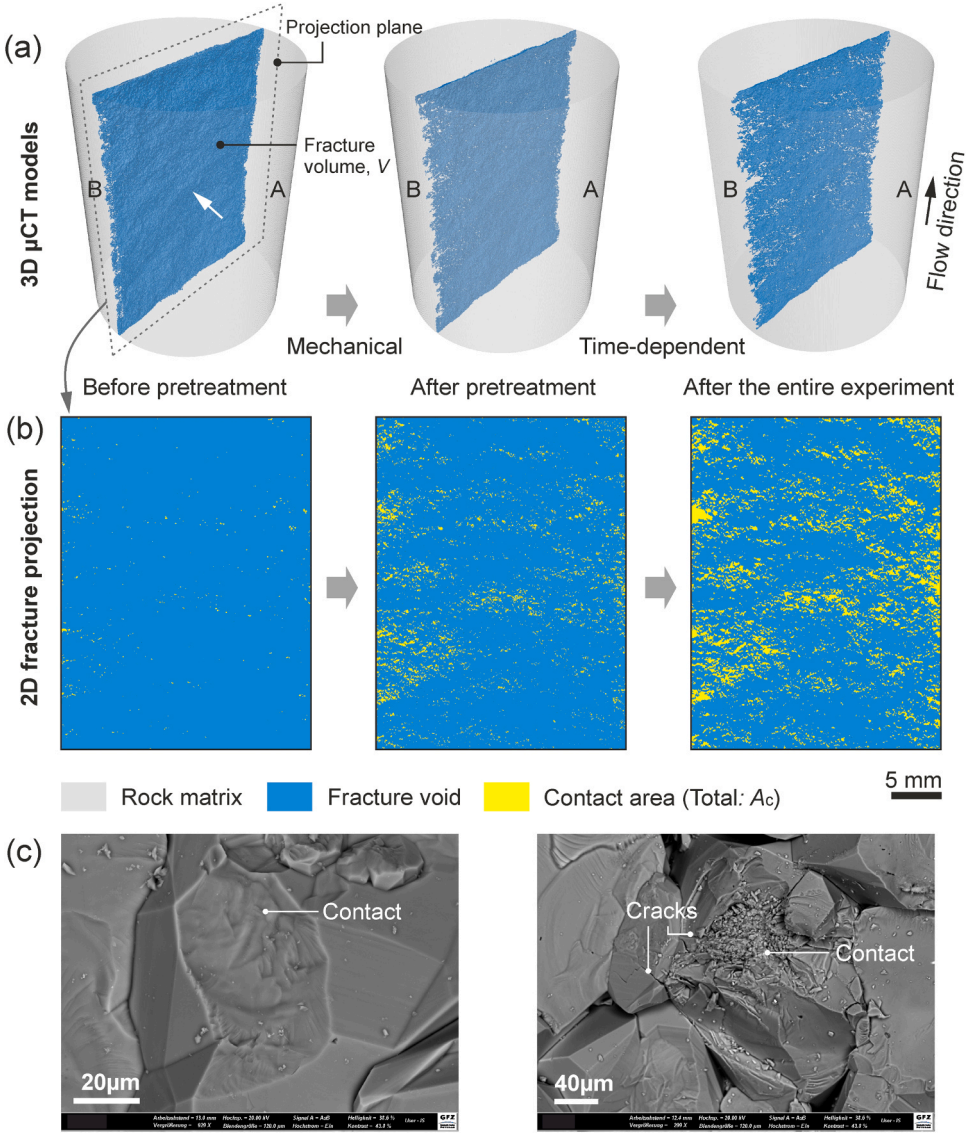



**Fig. 4.** (a) X-ray μCT-based 3-D perspective models obtained at different experimental stages. (b) 2-D projections of the extracted fracture with the fracture void (in blue) and the contact areas (in yellow) for the same stages. (c) SEM backscattered electron (BSE) micrographs of representative contact asperities after the experiment.

Consequently, the μCT-derived contact areas and contact numbers are meant to relatively compare the morphological evolution rather than to derive absolute quantities. The increase in resolved contact area from 0.04 to 0.12 should therefore be interpreted as an indication of increasing contact area during the experiment, while its absolute magnitude is subject to the resolution and stress-state limitations.

## 4. Discussion

Despite a comprehensive knowledge base resulting from similar experiments that have been performed in the past (Section 1), only two studies can be identified that permit a direct comparison with the present investigation in terms of sample mineralogy, environmental conditions, and test duration, i.e., Polak et al.[3] and Yasuhara et al.[4]. The present study is unique though with respect to the relative displacement of the fracture halves, the continuous fluid flow at one defined and constant flow rate and temperature, the pressure conditions, as well as the dense analysis of the effluent chemistry for Si content. It is striking that the here observed overall trend in aperture decrease during the experiment including the deceleration of fracture closure after approximately half of the test is very similar to what was observed by Polak et al.[3]. Some degree of aperture increase as found by Yasuhara et al.[4] is evidently related to an increased quartz dissolution rate at temperatures above 100 °C and the very low (i.e., 1.4 MPa) effective pressure applied. This indicates that any contribution of free face dissolution that would yield an increase in fracture aperture is readily overprinted by fracture closure as effective pressure is increased.

This section discusses the key observations of the experiment which will be related to the three grain-scale mechanisms outlined in Section 1 (FFD, PS, and SCC), supported by the microstructural investigations (μCT and SEM). The concurrent measurements of hydraulic fracture aperture and effluent Si concentration will prove helpful in this regard (Fig. 3). It should be noted at this point that any experimental artifacts related to (metal) corrosion within the pore fluid system can be excluded due to the use of corrosion resistant materials (i.e., Hastelloy C-276). Moreover, mineral precipitation within the fracture void space is unlikely as, throughout the experiment, the bulk pore fluid was undersaturated with respect to dissolved Si. It should finally be emphasized that the following assessment remains semi-quantitative as the valuable lessons learned from this study suggest a number of follow-up investigations outlined in Section 5.

### 4.1. Free face dissolution (FFD)

The first primary observation is that the effluent Si concentration converges to some approximately constant value (i.e., a baseline) that is larger than the Si concentration in the injection fluid (stage IV onwards; Fig. 3d). This is a strong indication that FFD occurs throughout the entire experiment as fluid continuously flows through the fracture at constant temperature and pore pressure. A detailed calculation of the possible Si release by FFD is provided as supporting information in **Text S1**. It shows, that the calculated amount of Si release is in excellent agreement with the measured concentration difference between inlet and outlet when one assumes that predominantly amorphous silica, either preexisting or produced during initial sample splitting, is dissolved. Counterintuitively, there is no indication of an increase in hydraulic fracture aperture that one might expect when the fracture walls undergo dissolution. However, if one assumes that dissolution also occurs on the outer surfaces of the contacting asperities, this would progressively decrease their load bearing capacity yielding some degree of fracture closure. The slow reduction of hydraulic aperture between 1300 and 2300 h (stage IV; Fig. 3a) might be related to this mechanism and thus indirectly to FFD, then operating exclusively.

### 4.2. Pressure solution (PS) and stress corrosion cracking (SCC)

The second fundamental observation is that there are transient stages of hydraulic aperture decrease that can occur either with or without a noticeable increase in effluent Si concentration above the baseline mentioned in the previous subsection. This is evident for stage II as opposed to early stage III. In both cases the pore fluid was deionized water. It is suggested that PS dominates fracture deformation during the former stage and SCC during the latter. The essence of PS is the release of dissolved matter into the free pore fluid (e.g.,[22,49]). In contrast, although SCC is a chemo-mechanical process, it should only insignificantly affect the pore fluid Si concentration because it occurs at the crack tips, where the mineral bonds in the crystal lattice are replaced by weaker hydrogen bonds (e.g.,[14]). The contrasting microstructures of the two contacts shown in Fig. 4c support the interpretation that both PS and SCC may have occurred during the experiment, at least as long as the contact area ratio is below a certain threshold. It is noted though that the brittle features shown in Fig. 4c might have been introduced during preconditioning and/or during the loading stages, which will require additional tests followed by microstructural imaging to separate purely mechanical damage from fluid induced SCC. Moreover, the fracture surface scans shown in Figure S2 did not permit to identify PS features (e.g., precipitates) and/or to discriminate brittle asperity damage induced during preconditioning from SCC. This is obvious when comparing the before-after images but also results from the x-y resolution of the instrument which is low (ca. 24 μm) compared to the one required (Fig. 4c) rendering the evaluation of an image superposition difficult. Towards the end of the experiment (stage VII), a further increase in effective pressure had nearly no effect on hydraulic aperture. However, the elastic pressure response of hydraulic aperture does not necessarily match the concurrent changes in mechanical aperture upon loading or unloading when the fracture void space morphology was altered by chemically mediated fluid-rock interactions (e.g.,[50]). The existence of PS is further supported by the remarkable increase in effluent Si concentration during stage V, where unloading evidently yields a release of dissolved Si that was trapped within the asperity contacts. The local normal stress on the contacting asperities may not always be equivalent to the mean contact stress, i.e., $\sigma_c = (p_c - p_p)/R_c$ but might be variable across the fracture surface[51,52]. This could be the reason why some asperities that were in contact show fracturing, e.g., as a result of SCC, whereas some others preserve a microstructure that suggests occurrence of PS only (Fig. 4c).

### 4.3. Effects of changes in injection fluid composition

A third important observation is that the injection of a fluid that is rather close to saturation with respect to Si does not necessarily inhibit fracture deformation (stage III; Fig. 3a). PS is supposed to be a sequential process of dissolution, diffusion, and precipitation[8,9]. Thus, increasing the pore fluid Si concentration should decelerate the diffusion part of the overall process. In this experiment, the sudden increase in the pore fluid Si concentration should impede the mass transfer from the contact interfaces to the fracture void spaces and, as observed, hinder fracture deformation initially. Pore fluid Si could diffuse into the asperity contacts when there is an appropriate concentration gradient and the effluent Si concentration being first slightly lower than the one in the injection fluid could be an indication of this mechanism (Fig. 3c). As the non-hydrostatic quartz solubility is higher, the quartz dissolution kinetics is faster than under hydrostatic conditions[53] and the fluid in the void space is ca. 14% below saturation with respect to quartz (Section 2.1), during the second half of this stage, PS might reactivate, yielding both the observed decrease in hydraulic fracture aperture after approximately 600 h and the slight increase of the effluent Si concentration towards some new equilibrium. The observed trend in effluent Si concentration thus could have a physical meaning that, however, should not be over-interpreted as the minimum-maximum width of the effluent

signal is only approximately twice that of the influent data scatter. When flow with deionized water is reinstated (stage IV) fracture closure accelerates remarkably (Fig. 3a), which, when again attributed to PS, would be the result of the significantly increased concentration gradient. Consequently, the effluent Si concentration, as during stage II, is enhanced but shows a transient behavior (Fig. 3d) until after approximately 1300 h the Si level of the baseline (Section 4.1) is attained. From this point onwards, fracture deformation becomes controlled by FFD. Whether or not there is a concurrent or exclusive contribution of SCC to the overall decline of hydraulic fracture aperture during the Si-part of stage III is unclear. As during early stage III (deionized water) fracture deformation stopped, any contribution of SCC would imply that this mechanism is enhanced by Si-rich fluids at the crack tips. The authors could not find literature evidence that this is the case.

### 4.4. Deceleration of fracture closure

The fourth striking observation is the transient character of the changes in hydraulic fracture aperture and effluent Si concentration that seems inherent to both the response of the rock-fluid system to imposed changes in conditions as well as the global trend throughout the experiment. Ultimately, i.e., after about 1300 h, any dynamics of fracture deformation and Si content in the pore fluid is likely controlled by FFD. It remains to be disclosed why the preceding dominance of PS and/or SCC ceases at this point and could not be reactivated during stage VII. The μCT observations evidence (i) a significant increase in the contact area ratio during the experiment from 0.04 to 0.12 and (ii) an enlargement of the area of individual contacts (Figures 4b and S3). This results both in a decrease in mean contact stress and an increase in the diffusion length within the contact interfaces. Overall, for PS, this implies a decrease in the fracture-normal creep rate (e.g.,[22,27,49]). Whether there is a threshold stress, below which pressure solution ceases, however, is an ongoing debate[54,55]. For SCC, a critical effective pressure may exist, below which crack propagation would not occur[56]. It is noted though that a variability of the rate at which hydraulic aperture decreases at otherwise unchanged conditions cannot be mechanistically assessed at this point. Moreover, the three μCT scans in Fig. 4 provide only discrete snapshots of the fracture morphology and therefore cannot directly resolve the evolution of the contact area during the 2900 h experiment. The interpretation of a continuous deceleration of fracture closure is primarily based on the evolution of hydraulic aperture and effluent Si concentration during stage IV in Fig. 3. The μCT observations provide morphological evidence rather than direct measurements and support the interpretation of an overall increase in contact area. In particular, the transition at approximately 1300 h is inferred from the changes in hydraulic aperture and effluent Si concentration, not from an intermediate μCT measurement. The μCT results are used to provide a plausible structural explanation for the observed deceleration rather than to establish an exact timing by microstructural evidence.

## 5. Conclusions

The results of this flow-through experiment evidence that even at comparatively low temperatures and effective pressures (i.e., 60 °C and $< 30$ MPa) fractures in dense quartz-rich sandstones can undergo substantial closure (by ~50% in hydraulic aperture) within 4 months, with strong implications for fracture permeability. Compared to natural settings, this may have been favored by the use of deionized water as the pore fluid, but a significant contribution to the overall aperture decline was also observed when the pore fluid was close to saturation with respect to Si. In combination with the microstructural investigations performed it is suggested that, depending on the imposed conditions and the evolutionary state of fracture morphology, overall fracture deformation is controlled by a complex succession and/or combination of pressure solution, stress corrosion cracking, and free face dissolution. At some point, as both the total contact area and the diffusion path length within the asperity interfaces increase with time, both pressure solution and stress corrosion cracking halt and the dynamics of fracture closure then is suggested to be controlled exclusively by free face dissolution without obvious signs of reactivation of the former within the experimental effective pressure limits.

The present pressure and temperature conditions closely mimic the injection side of low to medium enthalpy deep geothermal energy systems. It is evident though that rock composition in sandstone reservoirs is more complex although quartz usually dominates. Before investigating effects of other major or minor minerals (e.g., K-feldspar, plagioclase, clays) the relative impact of the here outlined micromechanisms on fracture permeability requires a more quantitative assessment beyond the scope of this study. Based on the present observations and apart from more detailed theoretical considerations, appropriately designed experiments should be conducted to separate the respective processes and to conclude on their relative importance at given environmental conditions. Based on the present study it is suggested to replicate the experiment several times varying only one parameter at a time. (1) The pore fluid should be inert (e.g., decane) to separate purely mechanical from chemical processes; (2) the pore fluid should be deionized water and the experiment conducted at the lowest possible effective pressure (i.e., 1 MPa) to isolate any effect of free face dissolution; (3) and (4) again using deionized water as the pore fluid, two individual long-term experiments need to be performed at two different and elevated effective pressures to identify and separate the occurrence of pressure solution and stress corrosion cracking, respectively. The targeted pressures should be defined based on calculations as those detailed in Yasuhara and Elsworth[33]. Here, the evolution of the contact area ratio with time should receive particular attention as this would permit to derive the critical fracture-normal stresses below which pressure solution and stress corrosion cracking would respectively deactivate in support of the conclusions drawn in this study. This will also help to discriminate stress corrosion cracking from (ordinary) primary creep during transient changes in hydraulic aperture.

## Author contributions

CC designed and executed the experiment, performed the data treatment, evaluated the results, created the figures, and wrote parts of the manuscript draft. RL, HS, and OK advised on the experimental workflow and discussed the data. HM supervised and guided the study, provided analytical recommendations, evaluated and discussed the data, and edited the manuscript.

## Data availability

All experimental data were submitted to the GFZ Data Repository for public availability and can be freely accessed online at: https://doi.org/10.5880/GFZ.4.8.2020.007.

## Supporting materials

Supplementary information associated with this paper, as indicated in the main text, can be found online in the Supporting Materials.

## Funding

Financial support by the German Federal Ministry of Economics and Energy (BMWE; Grant No.: 0324244 C), the German Federal Ministry of Research, Technology and Space (BMFTR; Grant No.: 02NUK053E), and the Helmholtz Association (Grant No.: SO-093) is greatly acknowledged. This work is part of the Helmholtz Research Program "Changing Earth - Sustaining our Future", Topic 8 "Georesources for the Energy Transition and a High-Tech Society".

## CRediT authorship contribution statement

**Harald Milsch:** Writing – review & editing, Writing – original draft, Validation, Supervision, Resources, Project administration, Methodology, Funding acquisition, Conceptualization. **Chaojie Cheng:** Writing – original draft, Visualization, Validation, Methodology, Investigation, Formal analysis, Data curation, Conceptualization. **Renchao Lu:** Validation, Methodology, Formal analysis, Conceptualization. **Haibing Shao:** Validation, Methodology, Conceptualization. **Olaf Kolditz:** Validation, Methodology, Conceptualization.

## Declaration of Generative AI and AI-assisted technologies in the writing process

No generative AI was used in the manuscript preparation process.

## Declaration of Competing Interest

The authors declare that they have no known competing financial interests or personal relationships that could have appeared to influence the work reported in this paper.

## Acknowledgements

The authors wish to express their gratitude to Matthew Gill for assistance with the experiments and Jasper Florian Zimmermann and Michael Naumann (all at GFZ) for technical help with sample and specimen assembly preparation. Constructive reviews by two anonymous reviewers helped to improve the manuscript and are greatly acknowledged.

## Appendix A. Supporting information

Supplementary data associated with this article can be found in the online version at doi:10.1016/j.gete.2026.100924.

## Data availability

Data will be made available on request.

## References

1. Durham WB, Bourcier WL, Burton EA. Direct observation of reactive flow in a single fracture. *Water Resour Res*. 2001;37(1):1–12. https://doi.org/10.1029/2000WR900228.
2. Morrow CA, Moore DE, Lockner DA. Permeability reduction in granite under hydrothermal conditions. *J Geophys Res*. 2001;106(B12):30551–30560. https://doi.org/10.1029/2000jb000010.
3. Polak A, Elsworth D, Yasuhara H, Grader AS, Halleck PM. Permeability reduction of a natural fracture under net dissolution by hydrothermal fluids. *Geophys Res Lett*. 2003;30(20):2020. https://doi.org/10.1029/2003GL017575.
4. Yasuhara H, Polak A, Mitani Y, Grader A, Halleck P, Elsworth D. Evolution of fracture permeability through fluid–rock reaction under hydrothermal conditions. *Earth Planet Sci Lett*. 2006;244(1-2):186–200. https://doi.org/10.1016/j.epsl.2006.01.046.
5. Yasuhara H, Kinoshita N, Ohfuji H, Takahashi M, Ito K, Kishida K. Long-term observation of permeability in sedimentary rocks under high-temperature and stress conditions and its interpretation mediated by microstructural investigations. *Water Resour Res*. 2015;51(7):5425–5449. https://doi.org/10.1002/2014WR016427.
6. Hofmann H, Blocher G, Milsch H, Babadagli T, Zimmermann G. Transmissivity of aligned and displaced tensile fractures in granitic rocks during cyclic loading. *Int J Rock Mech Min Sci*. 2016;87:69–84. https://doi.org/10.1016/j.ijrmms.2016.05.011.
7. Beeler N, Hickman S. Stress-induced, time-dependent fracture closure at hydrothermal conditions. *J Geophys Res Solid Earth*. 2004;109(B2). https://doi.org/10.1029/2002JB001782.
8. Paterson M. Nonhydrostatic thermodynamics and its geologic applications. *Rev Geophys*. 1973;11(2):355–389. https://doi.org/10.1029/RG011i002p00355.
9. Weyl PK. Pressure solution and the force of crystallization: a phenomenological theory. *J Geophys Res*. 1959;64(11):2001–2025. https://doi.org/10.1029/JZ064i011p02001.
10. Yasuhara H, Elsworth D, Polak A. Evolution of permeability in a natural fracture: significant role of pressure solution. *J Geophys Res*. 2004;109(B3):B03204. https://doi.org/10.1029/2003JB002663.
11. Polak A, Elsworth D, Liu J, Grader AS. Spontaneous switching of permeability changes in a limestone fracture with net dissolution. *Water Resour Res*. 2004;40:W03502. https://doi.org/10.1029/2003WR002717.
12. Heap M, Baud P, Meredith P. Influence of temperature on brittle creep in sandstones. *Geophys Res Lett*. 2009;36(19). https://doi.org/10.1029/2009GL039373.
13. Heap M, Baud P, Meredith P, Bell A, Main I. Time-dependent brittle creep in Darley Dale sandstone. *J Geophys Res Solid Earth*. 2009;114(B7). https://doi.org/10.1029/2008JB006212.
14. Brantut N, Heap M, Meredith P, Baud P. Time-dependent cracking and brittle creep in crustal rocks: a review. *J Struct Geol*. 2013;52:17–43. https://doi.org/10.1016/j.jsg.2013.03.007.
15. Gratier J, Irigm RG. Experimental pressure solution-deposition on quartz grains: the crucial effect of the nature of the fluid. *J Struct Geol*. 1986;8(8):845–856. https://doi.org/10.1016/0191-8141(86)90030-1.
16. Lu R, Nagel T, Shao H, Kolditz O, Shao H. Modeling of dissolution-induced permeability evolution of a granite fracture under crustal conditions. *J Geophys Res Solid Earth*. 2018;123(7):5609–5627. https://doi.org/10.1029/2018JB015702.
17. Rutter E. The kinetics of rock deformation by pressure solution. *Trans R Soc Lond A*. 1976;283:203–219. https://doi.org/10.1098/rsta.1976.0079.
18. De Boer R. On the thermodynamics of pressure solution-interaction between chemical and mechanical forces. *Geochim Et Cosmochim Acta*. 1977;41(2):249–256. https://doi.org/10.1016/0016-7037(77)90232-0.
19. De Boer R, Nagtegaal P, Duyvis E. Pressure solution experiments on quartz sand. *Geochim Et Cosmochim Acta*. 1977;41(2):257–264. https://doi.org/10.1016/0016-7037(77)90233-2.
20. Gratier, J.-P., Dysthe, D.K., and Renard, F. (2013). The role of pressure solution creep in the ductility of the earth's upper crust, in Advances in Geophysics. edited by Dmowska, R., pp. 47-179, Elsevier. https://doi.org/10.1016/B978-0-12-380940-7.00002-0.
21. Schutjens PM. Experimental compaction of quartz sand at low effective stress and temperature conditions. *J Geol Soc*. 1991;148(3):527–539. https://doi.org/10.1144/gsjgs.148.3.0527.
22. Elias BP, Hajash JA. Changes in quartz solubility and porosity due to effective stress: An experimental investigation of pressure solution. *Geology*. 1992;20(5):451–454. https://doi.org/10.1130/0091-7613(1992)020<0451:CIQSAP>2.3.CO;2.
23. Niemeijer A, Spiers C, Bos B. Compaction creep of quartz sand at 400–600 °C: Experimental evidence for dissolution-controlled pressure solution. *Earth Planet Sci Lett*. 2002;195(3-4):261–275. https://doi.org/10.1016/S0012-821X(01)00593-3.
24. Van Noort R, Spiers CJ, Pennock GM. Compaction of granular quartz under hydrothermal conditions: controlling mechanisms and grain boundary processes. *J Geophys Res*. 2008;113(B12):B12206. https://doi.org/10.1029/2008JB005815.
25. De Meer S, Spiers CJ, Peach CJ, Watanabe T. Diffusive properties of fluid-filled grain boundaries measured electrically during active pressure solution. *Earth Planet Sci Lett*. 2002;200(1-2):147–157. https://doi.org/10.1016/S0012-821X(02)00585-X.
26. Dysthe DK, Renard F, Feder J, Jamtveit B, Meakin P, Jossang T. High-resolution measurements of pressure solution creep. *Phys Rev E*. 2003;68(1), 011603. https://doi.org/10.1103/PhysRevE.68.011603.
27. Gratier JP, Guiguet R, Renard F, Jenatton L, Bernard D. A pressure solution creep law for quartz from indentation experiments. *J Geophys Res*. 2009;114(B3):B03403. https://doi.org/10.1029/2008JB005652.
28. Gratier JP, Renard F, Vial B. Postseismic pressure solution creep: evidence and time-dependent change from dynamic indenting experiments. *J Geophys Res Solid Earth*. 2014;119(4):2764–2779. https://doi.org/10.1002/2013JB010768.
29. Sanchez-Roa C, Saldi GD, Mitchell TM, et al. The role of fluid chemistry on permeability evolution in granite: applications to natural and anthropogenic systems. *Earth Planet Sci Lett*. 2021. https://doi.org/10.1016/j.epsl.2020.116641.
30. Anderson OL, Grew PC. Stress corrosion theory of crack propagation with applications to geophysics. *Rev Geophys*. 1977;15(1):77–104. https://doi.org/10.1029/RG015i001p00077.
31. Atkinson BK. Subcritical crack growth in geological materials. *J Geophys Res Solid Earth*. 1984;89(B6):4077–4114. https://doi.org/10.1029/JB089iB06p04077.
32. Heap M, Baud P, Meredith P, Vinciguerra S, Bell A, Main I. Brittle creep in basalt and its application to time-dependent volcano deformation. *Earth Planet Sci Lett*. 2011;307(1-2):71–82. https://doi.org/10.1016/j.epsl.2011.04.035.
33. Yasuhara H, Elsworth D. Compaction of a rock fracture moderated by competing roles of stress corrosion and pressure solution. *Pure Appl Geophys*. 2008;165(7):1289–1306. https://doi.org/10.1007/s00024-008-0356-2.
34. Farough A, Moore DE, Lockner DA, Lowell R. Evolution of fracture permeability of ultramafic rocks undergoing serpentinization at hydrothermal conditions: An experimental study. *Geochem Geophys Geosystems*. 2016;17(1):44–55. https://doi.org/10.1002/2015gc005973.
35. Ishibashi T, McGuire TP, Watanabe N, Tsuchiya N, Elsworth D. Permeability evolution in carbonate fractures: competing roles of confining stress and fluid pH. *Water Resour Res*. 2013;49(5):2828–2842. https://doi.org/10.1002/wrcr.20253.
36. Kamali-Asl A, Ghazanfari E, Perdrial N, Cladouhos T. Effects of injection fluid type on pressure-dependent permeability evolution of fractured rocks in geothermal reservoirs: an experimental chemo-mechanical study. *Geothermics*. 2020;87,101832. https://doi.org/10.1016/j.geothermics.2020.101832.
37. Marone C, Rubenstone J, Engelder T. An experimental study of permeability and fluid chemistry in an artificially jointed marble. *J Geophys Res*. 1988;93(B11):13763–13775. https://doi.org/10.1029/JB093iB11p13763.
38. Moore DE, Lockner DA, Byerlee JD. Reduction of permeability in granite at elevated temperatures. *Science*. 1994;265(5178):1558–1561. https://doi.org/10.1126/science.265.5178.1558.

39. Moore DE, Morrow C, Byerlee J. Chemical reactions accompanying fluid flow through granite held in a temperature gradient. *Geochim Et Cosmochim Acta*. 1983; 47(3):445–453. https://doi.org/10.1016/0016-7037(83)90267-3.
40. Morrow C, Lockner D, Moore D, Byerlee J. Permeability of granite in a temperature gradient. *J Geophys Res Solid Earth*. 1981;86(B4):3002–3008. https://doi.org/10.1029/JB086iB04p03002.
41. Cheng C, Milsch H. Evolution of fracture aperture in quartz sandstone under hydrothermal conditions: mechanical and chemical effects. *Minerals*. 2020;10(8): 657. https://doi.org/10.3390/min10080657.
42. Yasuhara H, Kinoshita N, Ohfuji H, Lee DS, Nakashima S, Kishida K. Temporal alteration of fracture permeability in granite under hydrothermal conditions and its interpretation by coupled chemo-mechanical model. *Appl Geochem*. 2011;26(12): 2074–2088. https://doi.org/10.1016/j.apgeochem.2011.07.005.
43. Fournier RO, Potter II, RW. An equation correlating the solubility of quartz in water from 25 to 900C at pressures up to 10,000 bars. *Geochim Et Cosmochim Acta*. 1982;46 (10):1969–1973. https://doi.org/10.1016/0016-7037(82)90135-1.
44. Milsch H, Spangenberg E, Kulenkampff J, Meyhöfer S. A new apparatus for long-term petrophysical investigations on geothermal reservoir rocks at simulated in-situ conditions. *Transp Porous Media*. 2008;74(1):73–85. https://doi.org/10.1007/s11242-007-9186-4.
45. Witherspoon PA, Wang JS, Iwai K, Gale JE. Validity of cubic law for fluid flow in a deformable rock fracture. *Water Resour Res*. 1980;16(6):1016–1024. https://doi.org/10.1029/WR016i006p01016.
46. Renshaw CE. On the relationship between mechanical and hydraulic apertures in rough-walled fractures. *J Geophys Res*. 1995;100(B12):24629–24636. https://doi.org/10.1029/95JB02159.
47. Cheng C, Lu R, Shao H, Kolditz O, Milsch H. Data for a long-term flow-through experiment with a pure quartz Fontainebleau sandstone containing a macroscopic fracture performed at GFZ Potsdam. *GFZ Data Serv*. 2020. https://doi.org/10.5880/GFZ.4.8.2020.007.
48. Renard F, Beauprêtre S, Voisin C, et al. Strength evolution of a reactive frictional interface is controlled by the dynamics of contacts and chemical effects. *Earth Planet Sci Lett*. 2012;341-344:20–34. https://doi.org/10.1016/j.epsl.2012.04.048.
49. Dewers T, Hajash A. Rate laws for water-assisted compaction and stress-induced water-rock interaction in sandstones. *J Geophys Res*. 1995;100(B7):13093–13112. https://doi.org/10.1029/95JB00912.
50. Cheng, C., Hilgers, C., and Milsch, H. (2026). Time-dependent evolution of hydraulic and mechanical fracture apertures mediated by fluid-rock interactions. Abstract, CouFrac 2026 - 5th International Conference on Coupled Processes in Fractured Geological Media: Observation, Modeling, and Application. Uppsala, Sweden, 20-23 September 2026.
51. Kling T, Vogler D, Pastewka L, Amann F, Blum P. Numerical simulations and validation of contact mechanics in a granodiorite fracture. *Rock Mech Rock Eng*. 2018;51(9):2805–2824. https://doi.org/10.1007/s00603-018-1498-x.
52. Vogler D, Settgast RR, Annavarapu C, Madonna C, Bayer P, Amann F. Experiments and simulations of fully hydro-mechanically coupled response of rough fractures exposed to high-pressure fluid injection. *J Geophys Res Solid Earth*. 2018;123(2): 1186–1200. https://doi.org/10.1002/2017JB015057.
53. Renard F, Park A, Ortoleva P, Gratier J-P. An integrated model for transitional pressure solution in sandstones. *Tectonophysics*. 1999;312(2-4):97–115. https://doi.org/10.1016/S0040-1951(99)00202-4.
54. Neretnieks I. Stress-mediated closing of fractures: Impact of matrix diffusion. *J Geophys Res Solid Earth*. 2014;119(5):4149–4163. https://doi.org/10.1002/2013JB010645.
55. Revil A. Pervasive pressure-solution transfer: A poro-visco-plastic model. *Geophys Res Lett*. 1999;26(2):255–258. https://doi.org/10.1029/1998GL900268.
56. Zhang J, Wong TF, Davis DM. Micromechanics of pressure-induced grain crushing in porous rocks. *J Geophys Res Solid Earth*. 1990;95(B1):341–352. https://doi.org/10.1029/JB095iB01p00341.